

# Extreme ultraviolet laser excitation of isotopic molecular nitrogen: The dipole-allowed spectrum of $^{15}\text{N}_2$ and $^{14}\text{N}^{15}\text{N}$

J. P. Sprengers<sup>a)</sup> and W. Ubachs

*Department of Physics and Astronomy, Laser Centre, Vrije Universiteit, De Boelelaan 1081, 1081 HV Amsterdam, The Netherlands*

K. G. H. Baldwin and B. R. Lewis

*Research School of Physical Sciences and Engineering, The Australian National University, Canberra, ACT, 0200, Australia*

W.-Ü L. Tchang-Brillet

*LERMA, UMR8112 du CNRS, Observatoire de Paris-Meudon, F-92195 Meudon Cedex, France and Université Pierre et Marie Curie (Paris 6), Paris, France*

(Received 24 March 2003; accepted 14 May 2003)

Extreme ultraviolet+ultraviolet (XUV+UV) two-photon ionization spectra of the  $b\ ^1\Pi_u(v=0-9)$ ,  $c_3\ ^1\Pi_u(v=0,1)$ ,  $o\ ^1\Pi_u(v=0,1)$ ,  $c_4'\ ^1\Sigma_u^+(v=1)$  and  $b'\ ^1\Sigma_u^+(v=1,3-6)$  states of  $^{15}\text{N}_2$  were recorded with a resolution of  $0.3\ \text{cm}^{-1}$  full-width at half-maximum (FWHM). In addition, the  $b\ ^1\Pi_u(v=1,5-7)$  states of  $^{14}\text{N}^{15}\text{N}$  were investigated with the same laser source. Furthermore, using an ultranarrow bandwidth XUV laser [ $\sim 250\ \text{MHz}$  ( $\sim 0.01\ \text{cm}^{-1}$ ) FWHM], XUV+UV ionization spectra of the  $b\ ^1\Pi_u(v=0-1,5-7)$ ,  $c_3\ ^1\Pi_u(v=0)$ ,  $o\ ^1\Pi_u(v=0)$ ,  $c_4'\ ^1\Sigma_u^+(v=0)$ , and  $b'\ ^1\Sigma_u^+(v=1)$  states of  $^{15}\text{N}_2$  were recorded in order to better resolve the band-head regions. For  $^{14}\text{N}^{15}\text{N}$ , ultrahigh resolution spectra of the  $b\ ^1\Pi_u(v=0-1,5-6)$ ,  $c_3\ ^1\Pi_u(v=0)$ , and  $b'\ ^1\Sigma_u^+(v=1)$  states were recorded. Rotational analyses were performed for each band, revealing perturbations arising from the effects of Rydberg-valence interactions in the  $^1\Pi_u$  and  $^1\Sigma_u^+$  states, and rotational coupling between the  $^1\Pi_u$  and  $^1\Sigma_u^+$  manifolds. Finally, a comprehensive perturbation model, based on the diabatic-potential representation used previously for  $^{14}\text{N}_2$ , and involving diagonalization of the full interaction matrix for all Rydberg and valence states of  $^1\Sigma_u^+$  and  $^1\Pi_u$  symmetry in the energy window  $100\ 000-110\ 000\ \text{cm}^{-1}$ , was constructed. Term values for  $^{15}\text{N}_2$  and  $^{14}\text{N}^{15}\text{N}$  computed using this model were found to be in good agreement with experiment. © 2003 American Institute of Physics. [DOI: 10.1063/1.1589478]

## I. INTRODUCTION

Molecular nitrogen dominates atmospheric absorption in the extreme ultraviolet (XUV) spectral region for wavelengths immediately below 100 nm.  $\text{N}_2$  shields the Earth's surface from XUV radiation through photodissociation, photoexcitation, and photoionization processes, in which the singlet *ungerade* ( $^1\Sigma_u^+$  and  $^1\Pi_u$ ) states play significant roles.<sup>1</sup> These processes occur predominantly in the upper-atmospheric layers above 100 km. At those altitudes, the singlet *ungerade* states are not only populated via photoexcitation, but also via electron-collision-induced excitation processes. Following excitation, competing emission and predissociation processes occur, their rates providing key inputs for models explaining the radiation budget of the Earth's atmosphere. Such processes are also important in the nitrogen-rich atmospheres of the satellites Titan and Triton, of Saturn and Neptune, respectively.

Predissociation of the singlet *ungerade* states is likely to occur via coupling with (pre-)dissociating valence states of triplet character.<sup>2,3</sup> However, the predissociation mechanisms and the singlet-triplet coupling are not understood at

present. The isotopic study of the singlet *ungerade* states reported here and in subsequent works is important for further characterization of the molecular potentials and interactions that must be included in realistic predissociation models for  $\text{N}_2$ . Laboratory investigations of the spectra and predissociation rates for different  $\text{N}_2$  isotopomers are also relevant to an understanding of differences in isotopic abundances in nitrogen-rich planetary atmospheres. For example, in the Earth's atmosphere, only 1 out of 273 nitrogen atoms is the heavier  $^{15}\text{N}$  isotope. On Titan,<sup>4</sup> the  $^{15}\text{N}$  atom is enriched 4.5 times compared to the Earth, while on Mars<sup>5,6</sup> the  $^{15}\text{N}$  enrichment factor is 1.6.

Molecular nitrogen is almost transparent in the visible and the ultraviolet domains. However, strong electric-dipole-allowed absorption occurs in the XUV region with  $\lambda \leq 100\ \text{nm}$ , down to the first ionization limit at 79.5 nm and beyond. Lefebvre-Brion,<sup>7</sup> Dressler,<sup>8</sup> and Carroll and Collins<sup>9</sup> showed that the allowed spectrum consists of transitions from the ground state  $X\ ^1\Sigma_g^+$  to the  $c_n'\ ^1\Sigma_u^+$  and  $c_n\ ^1\Pi_u$  Rydberg series converging on the ionic ground state  $X\ ^2\Sigma_g^+$ , where  $n$  is the principal quantum number, the  $o_n\ ^1\Pi_u$  Rydberg series converging on the  $A\ ^2\Pi_u$  state of the ion, and the valence states  $b'\ ^1\Sigma_u^+$  and  $b\ ^1\Pi_u$ . Potential-energy curves for the relevant electronic states of  $\text{N}_2$  are shown in Fig. 1. It should be noted

<sup>a)</sup>Electronic mail: arjan@nat.vu.nl

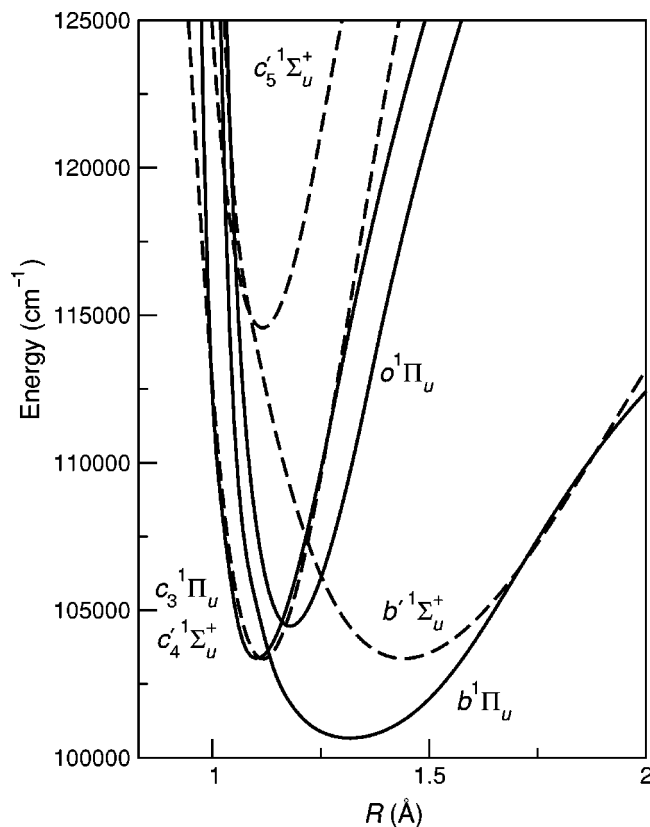


FIG. 1. Potential-energy curves for relevant singlet electronic states of  $N_2$ , shown in a diabatic (crossing) representation. Full curves:  ${}^1\Pi_u$  states. Dashed curves:  ${}^1\Sigma_u^+$  states. The energy scale is referenced to a zero defined by the  $v=0, J=0$  level of the  $X\ {}^1\Sigma_g^+$  state (not shown).

that there are alternative nomenclatures in use for some of these states. In particular,  $o_3$  is commonly known as  $o$ .

The  $N_2$  absorption spectrum in the XUV domain shows many irregularities, not only in the rovibronic structure, but also in the intensity distribution. Indeed, the spectrum was not understood for many years due to the complications introduced by strong interactions between the singlet *ungerade* states in this region. Stahel *et al.*<sup>10</sup> modeled the  $(c'_4, c'_5, \text{ and } b')\ {}^1\Sigma_u^+$  and  $(c_3, o, \text{ and } b)\ {}^1\Pi_u$  states in a diabatic representation and showed that the principal irregularities are due to homogeneous interactions within each of the two manifolds of states, mainly of Rydberg-valence type. Furthermore, heterogeneous interactions between the  ${}^1\Sigma_u^+$  and  ${}^1\Pi_u$  manifolds also add to the complexity of the spectra. Helm *et al.*,<sup>2</sup> Edwards *et al.*,<sup>11</sup> Walter *et al.*,<sup>12</sup> and Ubachs *et al.*<sup>13</sup> extended the work of Stahel *et al.*<sup>10</sup> by including these heterogeneous interactions in their calculations. The interactions between the  $c'_{n+1}\ {}^1\Sigma_u^+$  and  $c_n\ {}^1\Pi_u$  Rydberg states, which are members of  $p$  complexes, were analyzed using L-uncoupling theory by Carroll and Yoshino.<sup>14</sup> More recently, a comprehensive *ab initio* study of the three lowest  ${}^1\Sigma_u^+$  and  ${}^1\Pi_u$  states and their mutual interactions has been performed by Spelsberg and Meyer.<sup>15</sup>

The isotopomers  ${}^{14}N^{15}N$  and  ${}^{15}N_2$  have not been studied experimentally as extensively as the main isotopomer  ${}^{14}N_2$ . In the case of the  $X\ {}^1\Sigma_g^+$  state, accurate molecular constants for  ${}^{14}N_2$  and  ${}^{15}N_2$  were obtained in a high-resolution coher-

ent Raman spectroscopy experiment by Orlov *et al.*<sup>16</sup> while in a more recent Fourier-transform-Raman experiment, Bendtsen<sup>17</sup> determined the molecular constants of  ${}^{14}N^{15}N$  and  ${}^{15}N_2$  with even better accuracy.

In the case of the excited states in the XUV, the vibrational isotope shifts for  ${}^{15}N_2$  have been investigated by Ogawa *et al.*<sup>18,19</sup> in a classical absorption experiment. Yoshino *et al.*<sup>20</sup> measured the isotope shifts for the  $Q$  bandheads of the  $o_n\ {}^1\Pi_u (v=0-4)$  levels for both  ${}^{14}N^{15}N$  and  ${}^{15}N_2$ . Mahon-Smith and Carroll<sup>21</sup> measured vibrational isotope shifts for  ${}^{15}N_2$  in transitions between electronically-excited states. Rotationally-resolved spectra accessing the  $c'_4\ {}^1\Sigma_u^+ (v=0)$  and  $b'\ {}^1\Sigma_u^+ (v=1)$  levels of  ${}^{14}N^{15}N$  and  ${}^{15}N_2$  were recorded by Yoshino and Tanaka,<sup>22</sup> who analyzed the homogeneous interaction between these states for the different isotopomers. Hajim and Carroll<sup>23,24</sup> calculated the vibronic energies and the interaction energies of the  $c'_4\ {}^1\Sigma_u^+$  and  $b'\ {}^1\Sigma_u^+$  states of  ${}^{15}N_2$ ; their results were compared with unpublished results of Yoshino in Ref. 23.

In this article, an XUV+UV spectroscopic study of singlet *ungerade* states of the isotopomers  ${}^{14}N^{15}N$  and  ${}^{15}N_2$  in the 100 000–108 000  $\text{cm}^{-1}$  region is reported. While much of the study was performed with high resolution ( $\sim 3 \times 10^5$  resolving power), in some cases ultrahigh resolution was employed ( $\sim 10^7$  resolving power). Molecular parameters and isotope shifts have been determined from the rotationally-resolved spectra. Finally, using the model originally developed for  ${}^{14}N_2$  by Stahel *et al.*,<sup>10</sup> including heterogeneous interactions, we have computed term values for the relevant states of  ${}^{15}N_2$  and  ${}^{14}N^{15}N$ . Using the diabatic potential energy curves and couplings employed for  ${}^{14}N_2$ ,<sup>10</sup> we find good agreement between the experimental and computed results for  ${}^{15}N_2$  and  ${}^{14}N^{15}N$ . The present paper, one in a series, is intended to broadly summarize the isotopic results and identify the effects of the principal interactions. The original line assignments leading to the results presented here are available separately via the EPAPS data depository of the American Institute of Physics.<sup>25</sup> Future reports will focus on excited-state predissociation lifetimes and on the effects of singlet–triplet interactions in the XUV spectrum.

## II. EXPERIMENT

The experimental system has been described in detail elsewhere<sup>26,27</sup> and only the key features will be summarized here. We employ an XUV source which is based on harmonic upconversion, using two laser systems: a pulsed dye laser (PDL) with high resolution [XUV bandwidth  $\sim 9$  GHz ( $\sim 0.3\ \text{cm}^{-1}$ ) full-width at half-maximum (FWHM)] for undertaking survey spectra; and an ultrahigh resolution pulsed-dye-amplifier (PDA) yielding an XUV bandwidth of  $\sim 250$  MHz ( $\sim 0.01\ \text{cm}^{-1}$  FWHM) for measuring precise line positions and widths and to enable resolution of the congested band heads.

Both tunable pulsed laser systems, the PDL (Quanta-Ray PDL3), as well as the home-built PDA, are pumped by the second harmonic of a pulsed Nd:YAG laser. In such a system, a range of dyes can be used to cover a broad wavelength range in the red-yellow region with a short wavelength limit

of 545 nm. The PDA is injection seeded by the output of a Spectra Physics 380D cw-ring-dye laser, pumped by a cw 532 nm Millennia laser. In the configuration employed, the short-wavelength cut-off of this cw-system is at 566 nm, thereby also reducing the accessible wavelength range of the PDA.

The XUV radiation is generated in the same way for both laser systems, by frequency doubling the visible pulsed output in a KDP crystal, and then frequency tripling the resulting UV beam in a pulsed xenon jet. For the PDL and PDA sources, the lower wavelength limits in the XUV are 91 and 94.3 nm, respectively. At long wavelengths, both the PDL and PDA systems can be tuned to 600 nm, thus allowing the lowest dipole-allowed states in  $N_2$  to be accessed in the XUV near 100 nm.

The generated XUV beam and the UV beam propagate collinearly into the interaction chamber, where they are perpendicularly crossed with a skimmed and pulsed beam of  $N_2$ . For the measurements with the PDL system, the distance between the nozzle and the skimmer was decreased to only a few mm, in order to increase the number of  $N_2$  molecules in the interaction zone. In this way, the weaker bands of  $^{15}N_2$  and some strong bands of  $^{14}N^{15}N$  could be observed. For  $^{14}N^{15}N$ , only strong bands were observed because natural  $N_2$  gas was used, containing only 0.74%  $^{14}N^{15}N$ . For the  $^{15}N_2$  experiments, a 99.40%  $^{15}N$  isotopically enriched gas sample (Euriso-top) was used, enabling weak bands to be observed. For all PDL scans, the highest achievable laser power was used, i.e., 40 mJ/pulse in the UV, to enhance the signal of weak lines which otherwise could not be observed. In experiments with the ultrahigh resolution PDA source, the nozzle-skimmer distance was increased to a maximum of 150 mm to reduce the Doppler broadening, enabling more precise measurement of the transition frequencies and linewidths.

The  $N_2$  spectra were recorded using 1 XUV+1 UV two-photon ionization spectroscopy. The XUV photon excites the  $N_2$  molecules from the ground state to the states under investigation and, subsequently, the UV photon ionizes the molecule forming  $N_2^+$ , which is detected using a time-of-flight (TOF) electron-multiplier detection system. It should be noted that the signal intensities for the spectral lines recorded in 1 XUV+1 UV two-photon ionization do not directly reflect the cross sections of the single-XUV-photon-induced bound-bound transitions. The UV-laser-induced photoionization step also influences the signal intensities, particularly when autoionizing resonances are probed in the continuum above the ionization potential. No signatures of such resonances were found, however. Furthermore, the  $N_2^+$  signal intensity is strongly dependent on the lifetime of the intermediate (target) state. If the lifetime is shorter than the duration of the laser pulse (3 ns for XUV, 5 ns for UV), e.g., as a result of predissociation, the signal drops considerably. This phenomenon has been discussed in quantitative terms by Eikema *et al.*<sup>28</sup> The  $N_2^+$  ions are accelerated in the TOF apparatus, allowing for mass selective detection of the different isotopomers of  $N_2$  (masses 28, 29, and 30). Nevertheless, the signal of the much more abundant  $^{14}N_2$  was more than an order of magnitude higher than that of the  $^{14}N^{15}N$  isotopomer. In cases where the  $^{14}N^{15}N$  isotopomer has fea-

tures that spectrally coincide with  $^{14}N_2$  lines, the mass-selectivity is limited by the strong signal from the main isotopomer for two reasons: the large number of ions created give rise to a Coulomb explosion and the large mass-28 signals saturate the detector. In regions without spectral overlap the  $^{14}N^{15}N$  features were more favorably recorded.

The absolute frequency-calibration procedures employed have been discussed elsewhere for the PDL-based<sup>26</sup> and PDA-based<sup>29</sup> XUV sources. In both cases, frequency calibration is performed in the visible and the result is multiplied by a factor of 6 to account for the subsequent harmonic conversion. The frequency of the PDL is determined by simultaneously recording a Doppler-broadened  $I_2$  absorption spectrum which is compared with an iodine atlas.<sup>30</sup> The frequency of the PDA is determined by simultaneously recording fringes from a stabilized étalon (free spectral range 148.9567 MHz) and an  $I_2$  saturated-absorption spectrum, using the output of the cw-ring dye laser. Reference lines for the  $I_2$  spectrum are taken from an accurate list of saturated resonances produced in our laboratory<sup>31,32</sup> or from calculations.<sup>33</sup>

In some of the spectra recorded with the PDL source, line broadening associated with the ac-Stark effect was observed, sometimes yielding asymmetric line shapes. This phenomenon was not investigated in detail, but the ac-Stark-induced shifts were compensated for by comparison with spectra obtained using the PDA source. For several bands, low- $J$  lines were recorded with the PDA, while the entire band was recorded using the PDL at high laser intensity. Line positions from the PDA source were systematically lower by  $\Delta_{PDL-PDA} \approx 0.05-0.20 \text{ cm}^{-1}$ . Based on the observations with both systems, the PDL data were corrected for the ac-Stark shift, for those bands where ultrahigh resolution PDA data were available. Due to the uncertain Stark shifts, the absolute wave number uncertainty for the lines recorded with the PDL-based XUV source is  $\pm 0.2 \text{ cm}^{-1}$ , significantly worse than the calibration uncertainty of  $\pm 0.05 \text{ cm}^{-1}$ . The absolute calibration uncertainty for the PDA source is  $\pm 0.003 \text{ cm}^{-1}$ . This value represents a lower limit to the uncertainty for the narrowest spectral lines recorded. For lines where lifetime and/or Doppler broadening is of importance, the uncertainty is  $\pm 0.02 \text{ cm}^{-1}$ .

### III. ANALYSIS OF SPECTRA

Using the PDL system, rotationally-resolved spectra of transitions from  $X^1\Sigma_g^+(v=0)$  to the  $b^1\Pi_u(v=0-9)$ ,  $c_3^1\Pi_u(v=0,1)$ ,  $o^1\Pi_u(v=0,1)$ ,  $c_4'^1\Sigma_u^+(v=1)$ , and  $b'^1\Sigma_u^+(v=1,3-6)$  states of  $^{15}N_2$  and the  $b^1\Pi_u(v=1,5-7)$  states of  $^{14}N^{15}N$  were recorded. With the much narrower-bandwidth PDA source, spectra for transitions to the  $b^1\Pi_u(v=0-1,5-7)$ ,  $c_3^1\Pi_u(v=0)$ ,  $o^1\Pi_u(v=0)$ ,  $c_4'^1\Sigma_u^+(v=0)$ , and  $b'^1\Sigma_u^+(v=1)$  states of  $^{15}N_2$  and the  $b^1\Pi_u(v=0-1,5-6)$ ,  $c_3^1\Pi_u(v=0)$  and  $b'^1\Sigma_u^+(v=1)$  states of  $^{14}N^{15}N$  were recorded in order to resolve the band-head regions.

Since the nozzle-skimmer distance was increased in the PDA-based measurements, to minimize the Doppler width and improve the spectral resolution, the rotational tempera-

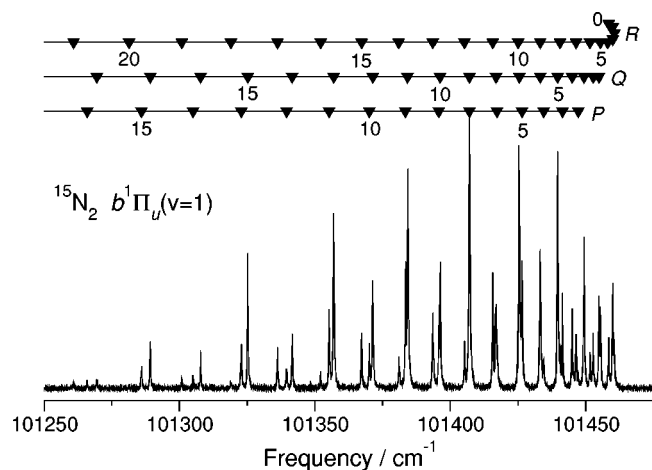


FIG. 2. 1 XUV+1 UV ionization spectrum and line assignments for the  $^{15}\text{N}_2$   $b^1\Pi_u-X^1\Sigma_g^+(1,0)$  band, recorded using PDL-based XUV source with a resolution of  $\sim 0.3\text{ cm}^{-1}$  (9 GHz) FWHM.

ture was low and transitions arising from only those ground-state levels with  $J'' \leq 5$  could be observed. The difference in resolution of the two laser systems is illustrated in Figs. 2 and 3, in which spectra of the  $b-X(1,0)$  band of  $^{15}\text{N}_2$ , recorded with the PDL source, and the  $b-X(5,0)$  band of  $^{15}\text{N}_2$  obtained with the PDA system, are shown, respectively. Linewidths of  $\sim 0.3\text{ cm}^{-1}$  FWHM are observed in the PDL-based recordings if the excited state is not severely predissociated. This value is predominantly due to the laser bandwidth, but includes a contribution from Doppler broadening and is independent of the specific nozzle-skimmer distance chosen. The linewidths for the PDA-based recordings are partially determined by the laser-source bandwidth (250 MHz FWHM) and partially by Doppler broadening which depends on the nozzle-skimmer distance. The minimum linewidth measured was 300 MHz FWHM, corresponding to the case of no predissociation.

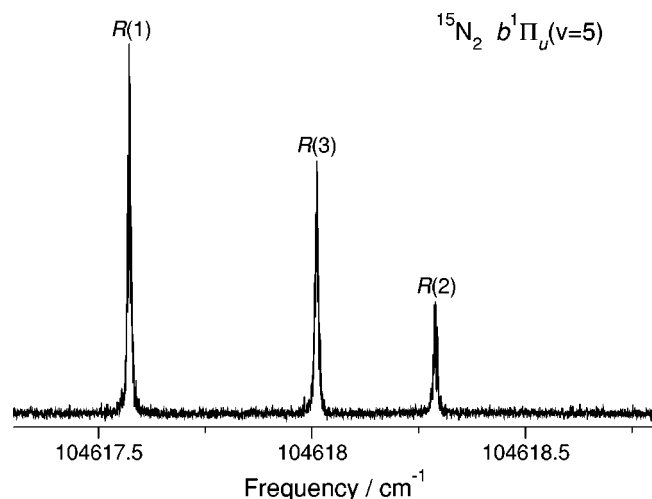


FIG. 3. 1 XUV+1 UV ionization spectrum of the  $^{15}\text{N}_2$   $b^1\Pi_u-X^1\Sigma_g^+(5,0)$  band-head region, recorded using PDA-based XUV source with a resolution of  $\sim 0.01\text{ cm}^{-1}$  ( $\sim 250$  MHz) FWHM. For this level, little lifetime broadening occurs and the observed linewidth reflects the instrumental width.

Rotational lines in the  $P$ ,  $Q$ , and  $R$  branches of all bands were assigned using ground-state combination differences and guidance provided by the effects of nuclear-spin statistics on the appearance of spectra. For  $^{14}\text{N}_2$ , the nuclear spin  $I=1$ , which results in a 2:1 intensity alternation of the even:odd rotational lines. Conversely, for  $^{15}\text{N}_2$   $I=1/2$  and the odd lines are three times stronger than the even lines. Because  $^{14}\text{N}^{15}\text{N}$  is not a homonuclear diatomic molecule, no intensity alternation occurs in this case. Rotational line assignments and corresponding wave numbers for all bands studied are listed in Tables which have been lodged with the EPAPS data depository of the AIP.<sup>25</sup> As an example, transition energies for the  $b^1\Pi_u-X^1\Sigma_g^+(1,0)$  band of  $^{15}\text{N}_2$  are listed in Table I.

Term values for the rovibrational levels of the excited  $^1\Sigma_u^+$  and  $^1\Pi_u$  states accessed in this work were determined from the experimental transition energies using  $X^1\Sigma_g^+(v=0)$  terms obtained from the spectroscopic constants of Bendtsen<sup>17</sup> for both  $^{15}\text{N}_2$  and  $^{14}\text{N}^{15}\text{N}$ . Effective spectroscopic parameters for the isotopomers were determined by least-squares fitting polynomial expressions in  $J$  to the experimental rotational terms. We eschew the use of the terminology “spectroscopic constant” in relation to the excited states considered here since, for the most part, the observed levels are significantly perturbed, thus limiting or removing the mechanical significance normally attributed to these constants. Moreover, for the same reason, the number of polynomial terms necessary to reproduce the experimental results to an acceptable accuracy was, in many cases, found to be greater than usual, and the values of the polynomial coefficients were dependent on the number of terms.

Therefore, in the case of the excited states with  $^1\Sigma_u^+$  symmetry, the terms are taken to have the form

$$T(J, e) = \nu_0 + Bx - Dx^2 + Hx^3 + H'x^4, \quad (1)$$

where  $x = J(J+1)$ ,  $\nu_0$  is the band origin,  $B$ ,  $D$ ,  $H$ , and  $H'$  are rotational parameters, and we note that all rotational levels are of  $e$  parity.<sup>34</sup> The terms for the excited states with  $^1\Pi_u$  symmetry are represented as

$$T(J, f) = \nu_0 + By - Dy^2 + Hy^3 + H'y^4, \quad (2)$$

for the  $f$ -parity levels, and

$$T(J, e) = T(J, f) + \Delta T_{ef}(J), \quad (3)$$

for the  $e$ -parity levels, where  $y = x - 1$  and the  $\Lambda$ -doubling is taken as

$$\Delta T_{ef}(J) = qy + q'y^2 + q''y^3 + q'''y^4, \quad (4)$$

where  $q$ ,  $q'$ ,  $q''$ , and  $q'''$  are  $\Lambda$ -doubling parameters. The  $e$  levels of the excited state are accessed in the  $P$ - and  $R$ -branch transitions ( $J = J'' - 1$  and  $J = J'' + 1$ , respectively), while the  $f$  levels are accessed in the  $Q$ -branch transitions ( $J = J''$ ), absent in the case of the  $^1\Sigma_u^+ - X^1\Sigma_g^+$  bands.

From the least-squares fits, spectroscopic parameters for the  $b^1\Sigma_u^+(v=1, 3-6)$  and  $c_4^1\Sigma_u^+(v=1)$  states of  $^{15}\text{N}_2$  and the  $b^1\Sigma_u^+(v=1)$  state of  $^{14}\text{N}^{15}\text{N}$  were determined and the results are listed in Table II. For the  $c_4^1\Sigma_u^+(v=0)$  state of  $^{15}\text{N}_2$ , only a few  $R(J)$  lines were measured with the PDA system, yielding, however, an accurate determination of the

TABLE I. Observed transition energies for the  $b^1\Pi_u-X^1\Sigma_g^+(1,0)$  band of  $^{15}\text{N}_2$ . 101 000  $\text{cm}^{-1}$  has to be added to listed values for transition energies. Wave numbers given to three decimal places are from narrow-bandwidth pulsed dye-laser (PDA) spectra, those to two decimal places are from pulsed dye-laser (PDL) spectra. Wave numbers derived from blended lines are flagged with an asterisk (\*), those from shoulders in the spectra by s, and those from weak features by w. Deviations from transition energies calculated using a least-squares fit of Eqs. (2)–(4) to the corresponding term values are also shown ( $\Delta_{\text{oc}} = \text{obs.} - \text{calc.}$ ). All values in  $\text{cm}^{-1}$ .

$J$	$R(J)$	$\Delta_{\text{oc}}$	$Q(J)$	$\Delta_{\text{oc}}$	$P(J)$	$\Delta_{\text{oc}}$
0	458.455	−0.004				
1	460.014s	0.009	454.737	−0.007		
2	460.465	0.001	452.565	−0.009	447.17	−0.14
3	459.890s	0.053	449.310	−0.009	441.35	−0.08
4	458.04	−0.08	444.88	−0.10	434.39	−0.07
5	455.336	0.016	439.57	0.02	426.39	−0.01
6	451.48	0.05	433.10*	0.07	417.13s	−0.13
7	446.35	−0.10	425.42	−0.01	406.99*	−0.05
8	440.40	0.03	416.80s	0.07	395.66s	−0.05
9	433.10*	−0.09	406.99*	0.04	383.30	−0.01
10	424.96s	0.03	396.12s	0.06	370.02	0.21
11	415.54	−0.02	384.09	0.01	355.18	−0.05
12	405.13	0.04	371.26	0.25	339.49	−0.05
13	393.44	−0.07	356.84	0.01	322.75	−0.01
14	380.86	0.03	341.52	−0.04	304.92	0.05
15	367.16	0.12	325.16	−0.01	285.91	0.01
16	352.05	−0.09	307.69	0.01	265.83	0.01
17	336.11	0.00	289.12	0.05	244.43	−0.19
18	318.90	−0.06	269.41	0.06	222.36	0.04
19	300.74	0.05	248.45	−0.06	198.91	0.00
20	281.30	0.01	226.51	−0.03	174.38w	0.01
21	260.79	0.03	203.34	−0.11	148.66	−0.06
22	239.04w	−0.04	179.22w	−0.01		
23	216.20	−0.07	153.84	−0.03	094.02w	−0.02
24			127.38w	0.01		
25	167.29w	0.10	099.78w	0.05		

band origin. Spectroscopic parameters for the  $^1\Pi_u$  states, obtained from the least-squares fits, are given in Table III, for  $^{15}\text{N}_2$ , and Table IV, for  $^{14}\text{N}^{15}\text{N}$ . Term values derived from the PDL-based measurements, as well as the more accurate data from the PDA-based source, were simultaneously included in the fitting routines, taking account of the PDL–PDA shift, and using proper weighting of the uncertainties.

The isotopic spectroscopic parameters in Tables II–IV display the effects of perturbations, just as in the well-known case of  $^{14}\text{N}_2$ . In our analysis, we have taken the following approach: (1) For the stronger perturbations, where level

crossings are not so apparent, we follow the rotational term series to as high a  $J$  value as possible, thus requiring additional polynomial terms in the fitting procedure. In these cases, of course, the electronic character of each level changes significantly over the full range of  $J$ . (2) For weaker perturbations, we follow the terms through the level crossing, neglecting the small range of  $J$  values around the perturbed crossing region. The ranges of  $J$  values included in the fits are indicated in Tables II–IV. Our principal aim is to provide spectroscopic parameters which enable the reproduction of the experimental term values over as wide a range of

TABLE II. Spectroscopic parameters for the  $^1\Sigma_u^+$  states of  $^{15}\text{N}_2$  and  $^{14}\text{N}^{15}\text{N}$ . All values in  $\text{cm}^{-1}$ .

Level	$B$	$D \times 10^6$	$H \times 10^8$	$H' \times 10^{10}$	$\nu_0^a$	$J_{\text{max}}^b$
$b'^1\Sigma_u^+(v=1)^{15}\text{N}_2$	1.073 34(18)	−29(6)			104 419.8989(12)	$R(8), P(5)$
$b'^1\Sigma_u^+(v=3)^{15}\text{N}_2$	1.079 7(4)	21.2(10)			105 824.40(3)	$R(19), P(17)$
$b'^1\Sigma_u^+(v=4)^c^{15}\text{N}_2$	1.168 3(21)	−155(22)	122(8)	−16.0 (10)	106 567.84(6)	$R(14), P(21)$
$b'^1\Sigma_u^+(v=5)^{15}\text{N}_2$	1.087 0(8)	23.3(84)	3.3(3)		107 227.45(4)	$R(25), P(27)$
$b'^1\Sigma_u^+(v=6)^{15}\text{N}_2$	1.132(1)	79(6)	6.3(9)		107 874.97(4)	$R(20), P(18)$
$c_4^1\Sigma_u^+(v=0)^{15}\text{N}_2$	1.789 02(7)	68 <sup>d</sup>			104 326.2679(9)	$R(3)$
$c_4^1\Sigma_u^+(v=1)^{15}\text{N}_2$	1.605(2)	19(12)	−122(4)	10.2 (3)	106 308.01(5)	$R(23), P(21)$
$b'^1\Sigma_u^+(v=1)^{14}\text{N}^{15}\text{N}$	1.112 4(3)	−7(7)			104 419.009(2)	$R(5), P(2)$

<sup>a</sup>Numbers in parentheses indicate  $1\sigma$  fitting uncertainties, in units of the last significant figure. Absolute uncertainties in band origins are higher (see discussion at end of Sec. II).

<sup>b</sup>Highest- $J'$  rotational-branch lines included in fit are indicated.

<sup>c</sup> $J=21, 22, 24, 26$  omitted from fit due to perturbation with  $c_4^1\Sigma_u^+(v=1)$  and  $c_3^1\Pi_u(v=1)$  states.

<sup>d</sup>Fixed at  $D$  constant of Yoshino and Tanaka (Ref. 22).

TABLE III. Spectroscopic parameters for the  ${}^1\Pi_u$  states of  ${}^{15}\text{N}_2$ . All values in  $\text{cm}^{-1}$ .

Level	$B$	$D \times 10^6$	$H \times 10^8$	$q \times 10^3$	$q' \times 10^6$	$\nu_0^a$	$J_{\max}^b$
$b {}^1\Pi_u(v=0)$	1.347 4(10)	36(7)		-0.8(9)		100 844.729(7)	$R(9), Q(11), P(8)$
$b {}^1\Pi_u(v=1)$	1.315 25(8)	13.45(14)		-0.01(4)		101 457.142(4)	$R(25), Q(25), P(23)$
$b {}^1\Pi_u(v=2)$	1.299 0(4)	20.5(12)		0.3(2)		102 130.22(2)	$R(19), Q(17), P(5)$
$b {}^1\Pi_u(v=3)$	1.292 8(3)	20.7(8)		-0.72(14)		102 819.18(2)	$R(19), Q(19), P(17)$
$b {}^1\Pi_u(v=4)^c$	1.320 5(4)	33.9(7)		-0.9(4)	-2.0(10)	103 486.74(3)	$R(21), Q(23), P(23)$
$b {}^1\Pi_u(v=5)^d$	1.342 8(3)	-43(3)	4.34(7)	14.3(3)	-3(4)	104 614.502(2)	$R(15), Q(18), P(16)$
$b {}^1\Pi_u(v=6)$	1.268 5(2)	-0.9(8)		1.6(2)		105 235.932(2)	$R(16), Q(14), P(12)$
$b {}^1\Pi_u(v=7)$	1.260 3(3)	-18.6(9)	10.6(1)	-0.15(20)	-5.5(5)	105 980.069(3)	$R(25), Q(23), P(25)$
$b {}^1\Pi_u(v=8)^e$	1.272 2(9)	-151(6)	9.2(10)	9.4(12)	-40(12)	106 764.76(4)	$R(21), Q(20), P(20)$
$b {}^1\Pi_u(v=9)$	1.156 7(4)	-5.5(14)		0.2(2)		107 445.12(3)	$R(17), Q(16), P(15)$
$c_3 {}^1\Pi_u(v=0)^f$	1.398 05(10)	40.21(13)	-0.72(4)	-16.37(14)	27.10(8)	104 071.346(8)	$R(26), Q(27), P(25)$
$c_3 {}^1\Pi_u(v=1)^g$	1.590 2(19)	168(12)	-18(3)	60(3)	-649(22)	106 450.34(7)	$R(21), Q(27), P(26)$
$o {}^1\Pi_u(v=0)^h$	1.582 2(3)	63.3(13)		-10.1(4)	43(3)	105 646.69(1)	$R(21), Q(17), P(14)$
$o {}^1\Pi_u(v=1)$	1.619 5(3)	7.3(6)		-0.6(3)	-7.0(9)	107 578.15(2)	$R(19), Q(22), P(21)$

<sup>a</sup>See footnote a to Table II.<sup>b</sup>See footnote b to Table II.<sup>c</sup> $J = 15e, 15f, 16f$  (rotational perturbation, see Sec. V B 3) are omitted from fit.<sup>d</sup> $H' = -1.7(2) \times 10^{-10}$ ,  $q'' = 9.8(1.3) \times 10^{-8}$ .<sup>e</sup> $q'' = 2.3(4) \times 10^{-7}$ ,  $q''' = -2.6(4) \times 10^{-10}$ .  $J = 4f, 5f, 6f$  are blended and omitted from fit.<sup>f</sup> $q'' = -1.56(4) \times 10^{-8}$ .<sup>g</sup> $H' = 1.35(17) \times 10^{-10}$ ,  $q'' = 1.55(6) \times 10^{-6}$ ,  $q''' = -1.08(4) \times 10^{-9}$ .  $J = 3-11$  for both  $e$  and  $f$  levels (rotational perturbation, see Sec. V B 5) omitted from fit.<sup>h</sup> $q'' = -1.10(5) \times 10^{-7}$ . Deperturbed (see Sec. V B 4).

rotation as possible, to a level of precision commensurate with the relative experimental uncertainties.

Specific effects of perturbations manifest in Tables II–IV include irregularities in vibrational spacings and  $B$  values, together with widely varying  $D$  and  $q$  values. Some of these effects are summarized in Fig. 4, and particular cases are discussed in more detail in Sec. V. Principally, they are caused by Rydberg-valence interactions within the  ${}^1\Pi_u$  and  ${}^1\Sigma_u^+$  manifolds, together with rotational coupling between these manifolds. In the simplest possible view, anomalously large values of  $D$ , e.g., for  $b(v=4)$  of  ${}^{15}\text{N}_2$  in Table III, indicate either homogeneous perturbation by a level with a smaller  $B$  value, or heterogeneous perturbation, both from above. Conversely, a negative  $D$  value, e.g., for  $b(v=8)$  of  ${}^{15}\text{N}_2$  in Table III, indicates either homogeneous perturbation by a level with a larger  $B$  value, or a heterogeneous perturbation, both from below. A large-magnitude  $\Lambda$ -doubling parameter  $|q|$  for a  ${}^1\Pi_u$  state indicates a significant heterogeneous interaction between the  ${}^1\Pi_u$   $e$ -level and one of the  ${}^1\Sigma_u^+$  states. In principle, the  ${}^1\Pi_u$   $f$ -levels could be shifted in interactions with  ${}^1\Sigma_u^-$  states, but such states have not been reported for the 100 000–110 000  $\text{cm}^{-1}$  region in  $\text{N}_2$ . Hence a positive  $q$ -value, e.g., for  $b(v=5)$  of  ${}^{15}\text{N}_2$  in Table III, signifies that the  ${}^1\Pi_u$  level is dominantly perturbed by a

lower-lying  ${}^1\Sigma_u^+$  level, while in case of a negative  $q$ -value, e.g., for  $c_3(v=0)$  of  ${}^{15}\text{N}_2$  in Table III, the most strongly interacting  ${}^1\Sigma_u^+$  level lies energetically above the  ${}^1\Pi_u$  level.

#### IV. THEORY

A theoretical framework within which the perturbations as well as the intensities in the dipole-allowed spectrum of  ${}^{14}\text{N}_2$  could be explained was published in the seminal paper by Stahel *et al.*<sup>10</sup> Vibronic matrix diagonalization and close-coupling methods were applied separately to three  ${}^1\Sigma_u^+$  ( $b', c'_4, c'_5$ ) states and three  ${}^1\Pi_u$  ( $b, c_3, o$ ) states in a diabatic representation. A perturbation model was built separately for each symmetry, taking into account the Rydberg-valence interactions. Later on, rotational coupling, i.e., heterogeneous interactions between states of  ${}^1\Sigma_u^+$  and  ${}^1\Pi_u$  symmetry, was included in extended models by Helm *et al.*,<sup>2</sup> Edwards *et al.*,<sup>11</sup> and Ubachs *et al.*<sup>13</sup> These models accounted for  $J$ -dependent effects and also the  $\Lambda$ -doubling in the  ${}^1\Pi_u$  states. In the present study, the procedures of Ref. 13 used for  ${}^{14}\text{N}_2$  have been applied to the  ${}^{15}\text{N}_2$  and  ${}^{14}\text{N}^{15}\text{N}$  isotopomers. The same RKR diabatic potentials generated from molecular constants given by Stahel *et al.*<sup>10</sup> and the same Rydberg-valence coupling strengths have been used,

TABLE IV. Spectroscopic parameters for the  ${}^1\Pi_u$  states of  ${}^{14}\text{N}^{15}\text{N}$ . All values in  $\text{cm}^{-1}$ .

Level	$B$	$D \times 10^6$	$H \times 10^8$	$q \times 10^3$	$q' \times 10^6$	$\nu_0^a$	$J_{\max}^b$
$b {}^1\Pi_u(v=5)$	1.388 3(2)	-24.2(3)	2.0(2)	8.6(4)	36.6(15)	104 658.273(5)	$R(8), Q(20), P(18)$
$b {}^1\Pi_u(v=6)$	1.315 6(3)	9(3)		1.1(2)		105 292.5305(7)	$R(8), Q(10), P(5)$
$b {}^1\Pi_u(v=7)$	1.296 0(7)	-24(4)		-0.6(4)		106 046.349(4)	$R(9), Q(14), P(12)$
$c_3 {}^1\Pi_u(v=0)$	1.455(2)	-6(8)		-24(2)		104 106.370(7)	$R(7), Q(2)$

<sup>a</sup>See footnote a to Table II.<sup>b</sup>See footnote b to Table II.

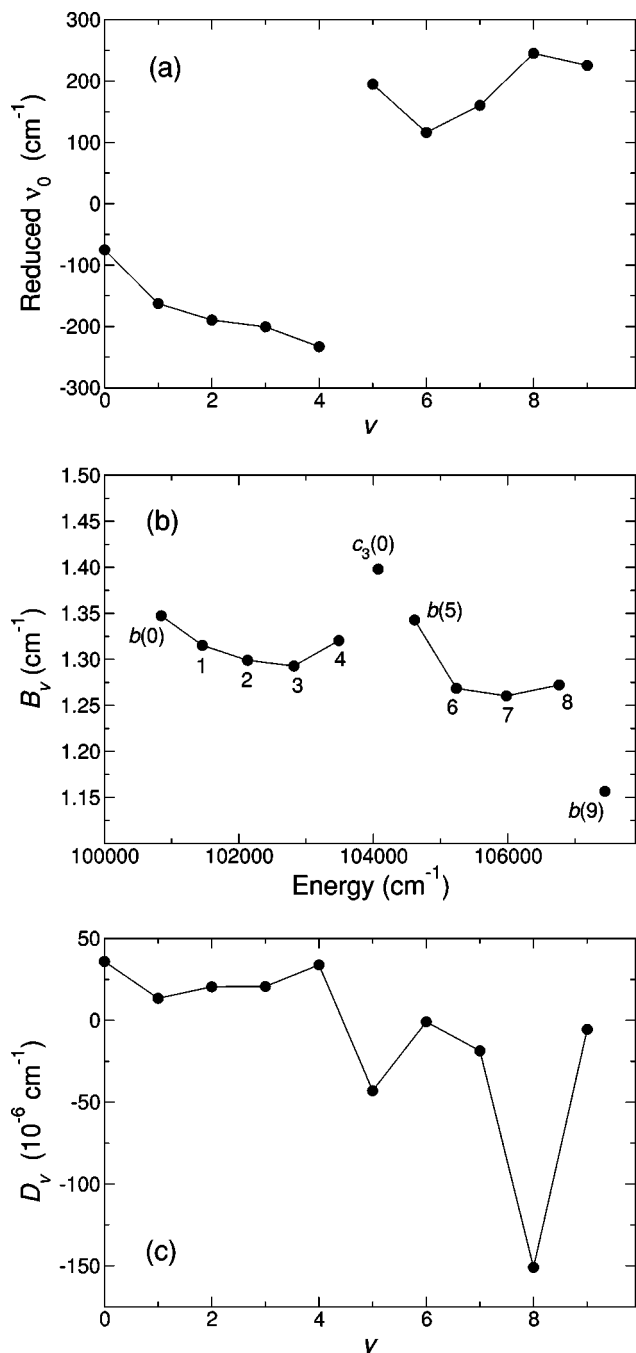


FIG. 4. Perturbations in the spectroscopic parameters of  $^{15}\text{N}_2$ . (a) Reduced band origins for  $b^1\Pi_u$  state. A linear term in  $v$  has been subtracted to emphasize the perturbations. (b)  $B$  values for the  $b^1\Pi_u$  and  $c_3^1\Pi_u(v=0)$  states. (c)  $D$  values for the  $b^1\Pi_u$  state.

since the diabatic potentials and coupling strengths, of electronic character, can be considered as invariant for different isotopomers. Thus, for each isotopomer and for each rotational quantum number  $J$ , coupled equations have been solved simultaneously for six states of both  $^1\Pi_u$  and  $^1\Sigma_u^+$  symmetries, with a centrifugal term added to the diabatic potentials and including only the most important heterogeneous interaction term  $-(\hbar^2/\mu R^2)\sqrt{J(J+1)}$  between the  $c_4'$  and  $c_3$  states. Both terms, being mass dependent, clearly vary with the isotopomer under consideration. This calculation provides the term values of the rotational  $e$  components of

the  $^1\Pi_u$  states, the only components affected by the heterogeneous interaction. To obtain the corresponding components of  $f$  symmetry, and consequently the  $\Lambda$ -doubblings of the  $^1\Pi_u$  states, a similar calculation has been performed for each  $J$ , with the same electronic coupling strengths, but without including the heterogeneous interaction term. The reduced masses used were  $\mu(^{15}\text{N}_2)=7.500\,054\,486\,5$  a.m.u. and  $\mu(^{14}\text{N}^{15}\text{N})=7.242\,226\,813$  a.m.u.<sup>35</sup> It is worth recalling that, as in Ref. 13, the Fourier grid Hamiltonian method,<sup>36</sup> an efficient and accurate method for bound state problems has been applied. The advantage of this method is in providing all the eigen values and the coupled-channels wave functions in one single diagonalization of the Hamiltonian matrix expressed in a discrete variable representation. As outlined previously,<sup>13</sup> for each energy value indexed by  $k$  and given  $J$ , the coupled-channels radial wave function is given by a six-component vector, each component corresponding to a given electronic diabatic state  $e$  ( $e=b, c_3, o, b', c_4', c_5'$ ):

$$\chi_k^d(R)=\{\chi_{ek}^d(R), \chi_{e'k}^d(R), \dots\}. \quad (5)$$

The percentage of the electronic character  $e$  is obtained directly by

$$P_e^k = \int_0^\infty |\chi_{ek}^d(R)|^2 dR. \quad (6)$$

The electronic component takes into account not only the bound vibrational states but also the vibrational continuum. The calculation for  $J=0$  yields the perturbed band origins. In principle, rotational parameters can be derived by fitting the results obtained for a set of  $J$  values to a polynomial. This has been done for a number of states during the course of analysis and some of these rotational parameters are given in Sec. V. However, for the most part, to be consistent with the case of  $^{14}\text{N}_2$ ,<sup>10</sup> the model rotational parameter  $B$  of each state has been calculated as the mean value of the operator  $h/8\pi^2c\mu R^2$  using the channel wave function with  $J=0$ . The model band origins and  $B$  values for  $^{15}\text{N}_2$  and  $^{14}\text{N}^{15}\text{N}$ , listed in Tables V and VI, respectively, are found to be in fairly good agreement with experiment, with deviations of the same order as found in the case of  $^{14}\text{N}_2$ .<sup>10</sup> The model rotational term values for  $^{15}\text{N}_2$  (curves) are compared in Fig. 5 with our experimental values (open circles). Inspection of Fig. 5 reveals the most prominent local interactions. Besides the well-known rotationally-dependent interaction between  $c_4'(0)$  and  $b'(1)$ ,<sup>22,29,37</sup> avoided crossings clearly occur between  $o(0)$  and  $b(7)$ , between  $o(0)$  and  $b'(3)$ , between  $c_3(1)$  and  $b(8)$ , and between  $b'(4)$  and  $c_4'(1)$ .

## V. DISCUSSION

### A. Isotope shifts

The vibrational isotope shifts for  $^{15}\text{N}_2$  and  $^{14}\text{N}^{15}\text{N}$  are defined as the band origin in  $^{14}\text{N}_2$  minus the band origin in  $^{15}\text{N}_2$  or  $^{14}\text{N}^{15}\text{N}$ , respectively. Isotope shifts derived from the present experimental measurements for the  $^1\Sigma_u^+$  and  $^1\Pi_u$  states are listed in Tables VII and VIII. In determining the isotope shifts, the band origins of  $^{14}\text{N}_2$  were taken from Ref. 37 for  $b'^1\Sigma_u^+(v=1)$  and  $c_4'^1\Sigma_u^+(v=0)$ , Ref. 38 for  $b'^1\Sigma_u^+(v=3-6)$  and  $c_4'^1\Sigma_u^+(v=1)$ , Ref. 39 for  $b^1\Pi_u(v$

TABLE V. Calculated band origins  $\nu_0$  and rotational parameters  $B$ , obtained from the comprehensive perturbation model, for the singlet ungerade states of  $^{15}\text{N}_2$ . Deviations  $\Delta$  from the experimental values are also indicated. All values in  $\text{cm}^{-1}$ .

Level	$\nu_0$ model	$\Delta\nu_0$ calc. - obs.	$B$ model	$\Delta B$ calc. - obs.
$b^1\Pi_u(v=0)$	100 838.088	-6.641	1.3130	-0.0344
$b^1\Pi_u(v=1)$	101 471.808	14.666	1.2996	-0.0157
$b^1\Pi_u(v=2)$	102 135.720	5.50	1.2885	-0.0105
$b^1\Pi_u(v=3)$	102 815.508	-3.67	1.2862	-0.0066
$b^1\Pi_u(v=4)$	103 483.531	-3.21	1.3158	-0.0047
$b'^1\Sigma_u^+(v=0)$	103 698.483		1.0803	
$c_3^1\Pi_u(v=0)$	104 075.404	4.058	1.4046	0.0065
$c_4^1\Sigma_u^+(v=0)$	104 329.699	3.431	1.7867	-0.0023
$b'^1\Sigma_u^+(v=1)$	104 416.495	-3.404	1.0741	0.0008
$b^1\Pi_u(v=5)$	104 608.546	-5.956	1.3673	0.0245
$b'^1\Sigma_u^+(v=2)$	105 127.642		1.0667	
$b^1\Pi_u(v=6)$	105 234.038	-1.894	1.2643	-0.0042
$o^1\Pi_u(v=0)$	105 661.170	14.48	1.5738	-0.0084
$b'^1\Sigma_u^+(v=3)$	105 826.844	2.44	1.0726	-0.0071
$b^1\Pi_u(v=7)$	105 965.810	-14.259	1.2443	-0.0160
$c_4^1\Sigma_u^+(v=1)$	106 306.961	-1.05	1.6498	0.045
$c_3^1\Pi_u(v=1)$	106 456.420	6.08	1.6307	0.0405
$b'^1\Sigma_u^+(v=4)$	106 565.300	-2.54	1.1408	-0.0275
$b^1\Pi_u(v=8)$	106 737.598	-27.16	1.2595	-0.0127
$b'^1\Sigma_u^+(v=5)$	107 230.487	3.04	1.0755	-0.0115
$b^1\Pi_u(v=9)$	107 438.341	-6.78	1.1568	0.0001
$o^1\Pi_u(v=1)$	107 575.750	-2.40	1.5845	-0.0350
$b'^1\Sigma_u^+(v=6)$	107 877.546	2.58	1.1291	-0.003
$b^1\Pi_u(v=10)$	108 157.169		1.1259	
$c_4^1\Sigma_u^+(v=2)$	108 381.354		1.3738	
$c_3^1\Pi_u(v=2)$	108 587.796		1.7210	
$b'^1\Sigma_u^+(v=7)$	108 792.718		1.2197	
$b^1\Pi_u(v=11)$	108 872.210		1.1060	
$b'^1\Sigma_u^+(v=8)$	109 386.783		1.0674	
$o^1\Pi_u(v=2)$	109 430.677		1.5419	
$b^1\Pi_u(v=12)$	109 578.467		1.0883	
$b'^1\Sigma_u^+(v=9)$	110 032.076		1.0375	
$b^1\Pi_u(v=13)$	110 255.672		1.0574	
$c_4^1\Sigma_u^+(v=3)$	110 486.892		1.6313	
$c_3^1\Pi_u(v=3)$	110 633.689		1.6700	

TABLE VI. Calculated band origins  $\nu_0$  and rotational parameters  $B$ , obtained from the comprehensive perturbation model, for the singlet ungerade states of  $^{14}\text{N}^{15}\text{N}$ . Deviations  $\Delta$  from the experimental values are also indicated. All values in  $\text{cm}^{-1}$ .

Level	$\nu_0$ model	$\Delta\nu_0$ calc. - obs.	$B$ model	$\Delta B$ calc. - obs.
$b^1\Pi_u(v=0)$	100 823.749		1.3595	
$b^1\Pi_u(v=1)$	101 469.292		1.3455	
$b^1\Pi_u(v=2)$	102 145.790		1.3339	
$b^1\Pi_u(v=3)$	102 838.068		1.3320	
$b^1\Pi_u(v=4)$	103 516.116		1.3660	
$b'^1\Sigma_u^+(v=0)$	103 684.821		1.1187	
$c_3^1\Pi_u(v=0)$	104 111.146	4.776	1.4606	0.006
$c_4^1\Sigma_u^+(v=0)$	104 327.640		1.8497	
$b'^1\Sigma_u^+(v=1)$	104 415.428	-3.581	1.1125	0.0001
$b^1\Pi_u(v=5)$	104 652.988	-5.285	1.4089	0.0206
$b'^1\Sigma_u^+(v=2)$	105 138.809		1.1045	
$b^1\Pi_u(v=6)$	105 292.593	0.063	1.3077	-0.0079
$o^1\Pi_u(v=0)$	105 670.635		1.6319	
$b'^1\Sigma_u^+(v=3)$	105 849.472		1.1117	
$b^1\Pi_u(v=7)$	106 037.459	-8.890	1.2821	-0.0139
$c_4^1\Sigma_u^+(v=1)$	106 337.397		1.7002	
$c_3^1\Pi_u(v=1)$	106 493.141		1.7025	
$b'^1\Sigma_u^+(v=4)$	106 604.364		1.1859	
$b^1\Pi_u(v=8)$	106 825.700		1.2812	
$b'^1\Sigma_u^+(v=5)$	107 279.719		1.1135	
$b^1\Pi_u(v=9)$	107 542.079		1.1941	
$o^1\Pi_u(v=1)$	107 605.417		1.6389	
$b'^1\Sigma_u^+(v=6)$	107 939.255		1.1656	
$b^1\Pi_u(v=10)$	108 271.946		1.1616	
$c_4^1\Sigma_u^+(v=2)$	108 457.126		1.4196	
$c_3^1\Pi_u(v=2)$	108 652.739		1.7804	
$b'^1\Sigma_u^+(v=7)$	108 869.575		1.2688	
$b^1\Pi_u(v=11)$	108 998.444		1.1396	
$b'^1\Sigma_u^+(v=8)$	109 469.218		1.1042	
$o^1\Pi_u(v=2)$	109 493.941		1.6056	
$b^1\Pi_u(v=12)$	109 711.747		1.1102	
$b'^1\Sigma_u^+(v=9)$	110 121.647		1.0772	
$b^1\Pi_u(v=13)$	110 399.274		1.0886	
$c_4^1\Sigma_u^+(v=3)$	110 574.578		1.6618	
$c_3^1\Pi_u(v=3)$	110 733.375		1.7331	

$=0$ ), Ref. 40 for  $b^1\Pi_u(v=1)$ , Ref. 9 for  $b^1\Pi_u(v=2-5,9)$ , Ref. 26 for  $b^1\Pi_u(v=6-8)$ , and  $o^1\Pi_u(v=0)$ , Ref. 37 for  $c_3^1\Pi_u(v=0)$ , Ref. 10 for  $c_3^1\Pi_u(v=1)$ , and Ref. 20 for  $o^1\Pi_u(v=1)$ . The band origins taken from some of these works<sup>9,10,20,26,37</sup> have been corrected to account for the different energy representation used previously.

In Tables VII and VIII, the isotope shifts are compared with literature values, and with values calculated using the perturbation model discussed in Sec. IV. The isotope shift of the corresponding band origin is negative for the  $b^1\Pi_u(v=0-1)$  levels because the isotope shift of the ground state  $X^1\Sigma_g^+(v=0, J=0)$  is larger than that of the excited states.

Reduced experimental  $^{14}\text{N}_2-^{15}\text{N}_2$  isotope shifts for vibrational levels of the  $b^1\Pi_u$  valence state, plotted in Fig. 6, are irregular, deviating from the smooth vibrational dependence expected for an unperturbed state. The experimental isotope-shift perturbations are in excellent agreement with our model calculations, which are also shown in Fig. 6 (note that the small systematic difference between the vibrational dependencies of the experimental and computed isotope shifts has been removed to facilitate this comparison of the

perturbation behavior). The isotope-shift perturbations become more noticeable for  $v \geq 4$ , where small shifts for the low- $v$  levels of the  $c_3$  Rydberg state, together with larger shifts for the higher- $v$  levels of the  $b$  state, result in differential effects which influence the pattern of Rydberg-valence energy degeneracies and consequent perturbation behavior.

Isotope shifts for the Rydberg  $^1\Pi_u$  states are also significantly perturbed, particularly for the  $v=0$  levels. An inspection of Table VIII shows  $^{14}\text{N}_2-^{15}\text{N}_2$  isotope shifts of 68.64 and 37.96  $\text{cm}^{-1}$ , respectively, for  $c_3(0)$  and  $o(0)$ , much higher than the near-zero value expected for an unperturbed  $v=0$  level. The positive perturbations observed in the low- $v$  Rydberg isotope shifts contrast with the predominantly negative perturbations found for the  $b^1\Pi_u$  valence levels of higher  $v$ , supporting the mutual Rydberg-valence nature of these perturbations.

## B. The $^1\Pi_u$ levels of $^{15}\text{N}_2$

The  $^1\Pi_u$  states of  $^{15}\text{N}_2$  undergo strong homogeneous interactions with each other and strong heterogeneous interactions with states of  $^1\Sigma_u^+$  symmetry. For most  $^1\Pi_u$  levels of

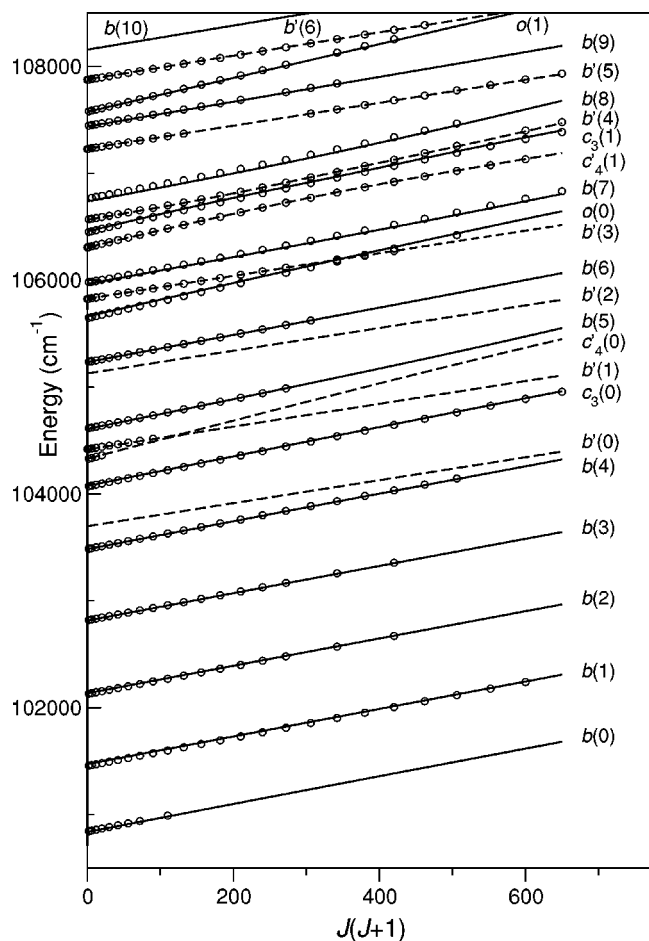


FIG. 5. Comparison between experimental and calculated rovibronic term values for the  ${}^1\Pi_u(e)$  and  ${}^1\Sigma_u^+$  states of  ${}^{15}\text{N}_2$ . Solid curves: calculated term values for the  ${}^1\Pi_u(e)$  states. Dashed curves: calculated term values for the  ${}^1\Sigma_u^+$  states. Open circles: experimental term values.

${}^{15}\text{N}_2$ , the perturbations are due to interactions with several other states and/or levels. Some distinction can be made between the strong vibronic interactions that cause entire rotational manifolds to be shifted by several hundreds of  $\text{cm}^{-1}$ ,

TABLE VIII. Isotope shifts of band origins for the  ${}^1\Pi_u$  states (see the text for  ${}^{14}\text{N}_2$  references). Observed shifts are compared with literature data and with the comprehensive perturbation model calculations. All values in  $\text{cm}^{-1}$ .

Level	${}^{15}\text{N}_2$ obs.	${}^{15}\text{N}_2$ previous	${}^{15}\text{N}_2$ model	${}^{14}\text{N}{}^{15}\text{N}$ obs.	${}^{14}\text{N}{}^{15}\text{N}$ model
$b^1\Pi_u(v=0)$	-26.466	-24.8 <sup>18</sup>	-28.35	-13.34 <sup>39</sup>	-14.04
$b^1\Pi_u(v=1)$	-4.140	-4.3 <sup>18</sup>	-4.88	-1.95 <sup>39</sup>	-2.40
$b^1\Pi_u(v=2)$	22.9	15.7 <sup>18</sup>	20.09		9.99
$b^1\Pi_u(v=3)$	45.8	39 <sup>18</sup>	44.84		22.24
$b^1\Pi_u(v=4)$	63.5	66.1 <sup>18</sup>	64.49		31.87
$b^1\Pi_u(v=5)$	87.1	89.3 <sup>18</sup>	88.22	43.4	43.74
$b^1\Pi_u(v=6)$	111.45	106.1 <sup>18</sup>	115.04	54.85	56.45
$b^1\Pi_u(v=7)$	130.90	137.4 <sup>18</sup>	141.88	64.62	70.20
$b^1\Pi_u(v=8)$	169.62	178 <sup>8</sup>	175.71		87.58
$b^1\Pi_u(v=9)$	199.6	182.6 <sup>18</sup>	209.70		105.93
$c_3^1\Pi_u(v=0)$	68.64	68.5 <sup>18</sup>	70.36	33.62	34.58
$c_3^1\Pi_u(v=1)$	79.2	79.7 <sup>18</sup>	73.44		36.68
$o^1\Pi_u(v=0)$	37.96	49.7 <sup>18</sup>	19.25	17.2 <sup>20</sup>	9.75
		37.8 <sup>20</sup>			
$o^1\Pi_u(v=1)$	61.1	70.6 <sup>18</sup>	54.72	41.9 <sup>20</sup>	25.02
		42.7 <sup>20</sup>			

such as the interaction between  $c_3^1\Pi_u(v=0)$  and the  $b^1\Pi_u$  levels, but there are also somewhat weaker interactions that give rise to local perturbations near crossing points. These points can be identified from the plot of term values in Fig. 5. In the following sections, these interactions are discussed for several groups of levels.

### 1. $b^1\Pi_u(v=0)$

As observed in the case of  ${}^{14}\text{N}_2$ ,<sup>9,39</sup> even allowing for considerable experimental uncertainty due to the low range of  $J$  values accessed, our  $D$  value for  ${}^{15}\text{N}_2$  is significantly higher than those observed for  $b(v=1,2)$ . Contrary to the suggestion of Carroll and Collins<sup>9</sup> that this effect is due to a strong perturbation of  $b(v=0)$  by an undetermined state, our calculations support the view that the high  $D$  value is a prop-

TABLE VII. Isotope shifts of band origins for the  ${}^1\Sigma_u^+$  states (see the text for  ${}^{14}\text{N}_2$  references). Observed shifts are compared with literature data and with the comprehensive perturbation model calculations. All values in  $\text{cm}^{-1}$ .

Level	${}^{15}\text{N}_2$ obs.	${}^{15}\text{N}_2$ previous	${}^{15}\text{N}_2$ model	${}^{14}\text{N}{}^{15}\text{N}$ obs.	${}^{14}\text{N}{}^{15}\text{N}$ previous	${}^{14}\text{N}{}^{15}\text{N}$ model
$b'^1\Sigma_u^+(v=1)$	-1.99	-1.0 <sup>23</sup> -2.0 <sup>22</sup> -0.3 <sup>18</sup>	-2.03	-1.10	-0.8 <sup>22</sup>	-1.00
$b'^1\Sigma_u^+(v=3)$	44.8	44.2 <sup>23</sup>	44.90			22.24
$b'^1\Sigma_u^+(v=4)$	79.1	79.9 <sup>23</sup> 80.2 <sup>18</sup>	77.69			38.59
$b'^1\Sigma_u^+(v=5)$	99.3	89.2 <sup>23</sup> 100.3 <sup>18</sup>	97.82			48.56
$b'^1\Sigma_u^+(v=6)$	124.3	123.8 <sup>23</sup> 129.3 <sup>18</sup>	122.65			60.90
$c_4^1\Sigma_u^+(v=0)$	-3.36	-3.4 <sup>23</sup> -3.5 <sup>22</sup>	-4.01		-1.7 <sup>22</sup>	-1.99
$c_4^1\Sigma_u^+(v=1)$	61.5	69.0 <sup>23</sup> 62.4 <sup>18</sup>	60.49			30.02

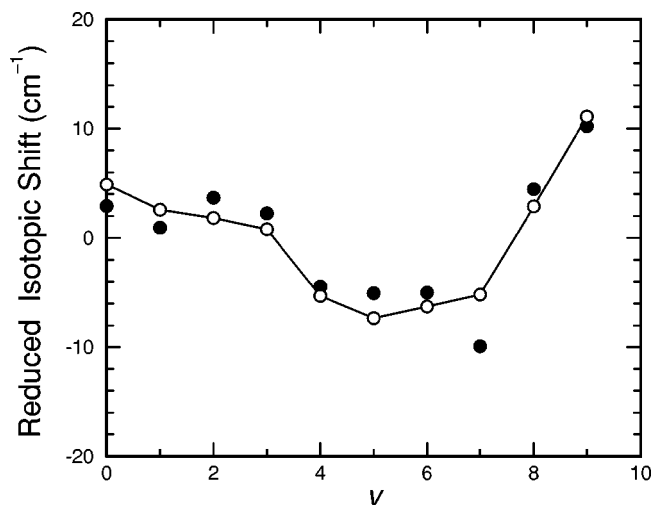


FIG. 6. Perturbations in the  $^{14}\text{N}_2$ - $^{15}\text{N}_2$  isotopic shifts for the  $b\ ^1\Pi_u$  state. Closed circles: Experimental. Open circles joined by solid lines: Model calculations. To facilitate presentation of the perturbations, the experimental and computed isotope shifts have been reduced by the subtraction of separate linear terms in  $v$ .

erty of the uncoupled  $b$ -state potential-energy curve, which has an unusual shape due to a configurational change near its minimum (see Fig. 1).<sup>15</sup>

## 2. $b\ ^1\Pi_u(v=1-3)$

There is no significant perturbation visible in the rotational structure of the  $b-X(1-3,0)$  bands. For example, the  $b\ ^1\Pi_u(v=1)$  level, which has been found to be well described by an unperturbed rotational progression for  $^{14}\text{N}_2$  by Ubachs *et al.*,<sup>39</sup> behaves similarly in the case of  $^{15}\text{N}_2$ , as shown in Table I. However, a global perturbation by the higher-lying  $c_3\ ^1\Pi_u$  state causes an overall shift of these  $b$ -state levels downwards by about  $200\text{ cm}^{-1}$ . This shift, however, has little effect on the rotational structure which can still be described using only two rotational parameters. According to Ref. 39, rotational levels of the  $^{14}\text{N}_2\ b\ ^1\Pi_u(v=3)$  state are diffuse and broadened due to the short lifetime of this level. As has been found elsewhere by Robbe,<sup>41</sup> the broadening of this level in  $^{15}\text{N}_2$  is much smaller than in  $^{14}\text{N}_2$ . The isotope-dependent lifetimes and predissociative behavior of the  $^1\Pi_u$  states will be discussed in detail in future publications.

## 3. $b\ ^1\Pi_u(v=4-5)$ and $c_3\ ^1\Pi_u(v=0)$

The  $b\ ^1\Pi_u(v=4-5)$  valence-state levels interact strongly with the  $c_3\ ^1\Pi_u(v=0)$  Rydberg level which lies between them. This homogeneous interaction pushes the  $b(4$  and  $5)$  levels downwards and upwards in energy, respectively, perturbing the corresponding origins as shown in Fig. 4(a). The perturbation model predicts for the  $b(4)$ ,  $b(5)$ , and  $c_3(0)$  states level shifts of  $-157.96$ ,  $+224.00$ , and  $-187.42\text{ cm}^{-1}$ , respectively, relative to their unperturbed positions (diabatic term values). The effects of the severe Rydberg-valence mixing are particularly noticeable in the  $B$  values, which are fairly similar for all three levels, as shown in Fig. 4(b) and as illustrated by the near-parallel term-value

plots in Fig. 5. In the absence of an interaction, the  $B$  value for  $c_3(0)$  predicted by the diabatic model is much higher:  $1.8277\text{ cm}^{-1}$ , characteristic of a  $v=0$  member of a Rydberg series converging on the ground state of the ion, while the predicted  $B$  values for  $b(4)$  and  $b(5)$  are much smaller:  $1.2278$  and  $1.2100\text{ cm}^{-1}$ , respectively. Furthermore, the same interaction is responsible for the widely differing  $D$  values for  $b(4)$ , which is significantly larger than expected for an unperturbed level, and for  $b(5)$ , which is of even greater magnitude and *negative*, as shown in Fig. 4(c).

There is also significant  $\Lambda$ -doubling in this region, which indicates heterogeneous interaction with  $^1\Sigma_u^+$  states. First, the  $b\ ^1\Sigma_u^+(v=0)$  state lies just above  $b(4)$ , shifting its  $e$  levels to lower energies, increasingly as  $J$  increases, while leaving the  $f$  levels unaffected, and resulting in a negative  $q$  value for  $b(4)$ . Second, as in  $^{14}\text{N}_2$ ,<sup>9</sup> the  $b(5)$  and  $c_3(0)$  states have relatively strong heterogeneous interactions with the  $c_4'(0)$  and  $b'(1)$  states, which lie between them. The result is that the  $e$  levels of the  $b(5)$  state are pushed upwards in energy and those of the  $c_3(0)$  state are shifted downwards. Therefore, the  $\Lambda$ -doubling parameter  $q$  is negative for  $c_3(0)$  and positive for  $b(5)$ , with almost the same magnitude. Fits of calculated rotational term values to Eqs. (2), (3), and (4), with the same numbers of  $J$  levels and parameters as in the experimental fits, lead to the following results for the  $B$ ,  $D$ , and  $q$  parameters: (1)  $b(4)$ :  $B = 1.3143\text{ cm}^{-1}$ ,  $D = 35.7 \times 10^{-6}\text{ cm}^{-1}$ , and  $q = -1.94 \times 10^{-3}\text{ cm}^{-1}$ . (2)  $b(5)$ :  $B = 1.3674\text{ cm}^{-1}$ ,  $D = -40.0 \times 10^{-6}\text{ cm}^{-1}$ , and  $q = 11.5 \times 10^{-3}\text{ cm}^{-1}$ . (3)  $c_3(0)$ :  $B = 1.4056\text{ cm}^{-1}$ ,  $D = 54.04 \times 10^{-6}\text{ cm}^{-1}$ , and  $q = -14.75 \times 10^{-3}\text{ cm}^{-1}$ . Overall, these parameters are in reasonably good agreement with those obtained from the experimental fits, given in Table III.

Finally, we note that we have observed new, weak local perturbations and extra lines in spectra of the  $b-X(4,0)$  band for both  $^{15}\text{N}_2$  and  $^{14}\text{N}_2$ . These perturbations occur in both the  $P$  and  $R$  branches [ $e$  levels of  $b(4)$ ] and in the  $Q$  branch ( $f$  levels), most prominently in the  $J=15e$  region for  $^{15}\text{N}_2$  and at  $J=18e$  for  $^{14}\text{N}_2$ . The latter perturbation has also been observed in synchrotron-based photoabsorption spectra by Stark.<sup>42</sup> There is no known singlet state of  $\text{N}_2$  energetically located so as to be able to cause these local perturbations, which will be assigned and analyzed elsewhere.

## 4. $b\ ^1\Pi_u(v=6-7)$ and $o\ ^1\Pi_u(v=0)$

The  $b\ ^1\Pi_u(v=6$  and  $7)$  valence levels interact with the  $o\ ^1\Pi_u(v=0)$  Rydberg level. As already mentioned by Yoshino *et al.*,<sup>20</sup> the interactions in  $^{14}\text{N}_2$  of  $o(0)$  with  $b(6$  and  $7)$  are equally strong, but opposite in sign. In contrast, in  $^{15}\text{N}_2$  the  $b(7)$  level lies closer to  $o(0)$  than does  $b(6)$ ,<sup>20</sup> resulting in much stronger interaction between  $b(7)$  and  $o(0)$  than between  $b(6)$  and  $o(0)$ . A plot of the experimental term values in the  $b(7)-o(0)$  region, shown in Fig. 7, demonstrates the effects of the avoided crossing between these two levels as the  $o(0)$  Rydberg level approaches the  $b(7)$  valence level from below with increasing  $J$ , including a tendency toward the two term series becoming parallel as the mixing increases. In fact, at  $J$  values higher than those in the avoided-crossing region ( $J > 25$ , according to the perturba-

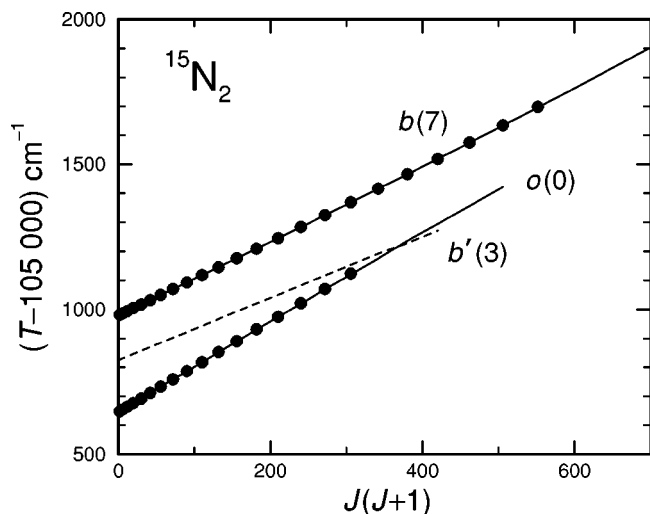


FIG. 7. Experimental rotational term values for the  $o(0)$ ,  $b(7)$ , and  $b'(3)$  states of  $^{15}\text{N}_2$ . Solid curves:  $^1\Pi_u(e)$  levels. Closed circles:  $^1\Pi_u(f)$  levels. Dashed curves:  $^1\Sigma_u^+$  ( $e$  levels only). A strongly-avoided Rydberg-valence crossing occurs between the  $o(0)$  and  $b(7)$  levels.

tion model) the upper term series, labeled  $b(7)$  in Fig. 7, has predominantly Rydberg character, while the lower has predominantly valence character. The same interaction is responsible for the negative  $D$  value for  $b(7)$ , the large  $D$  value for  $o(0)$ , and the need for a cubic polynomial to accurately represent the  $b(7)$  rotational terms (see Table III).

While the  $\Lambda$ -doubling in  $b(7)$  is small and regular, the heterogeneous interaction between  $o(0)$  and  $b'(3)$ , whose term series crosses that of  $o(0)$  from above, near  $J=19$ , results in significant perturbation of the  $e$  levels of  $o(0)$ , leaving the  $f$  levels untouched, as illustrated in Fig. 8, where we have also shown the results of a local two-level deperturbation of the  $e$ -level crossing region. Al-

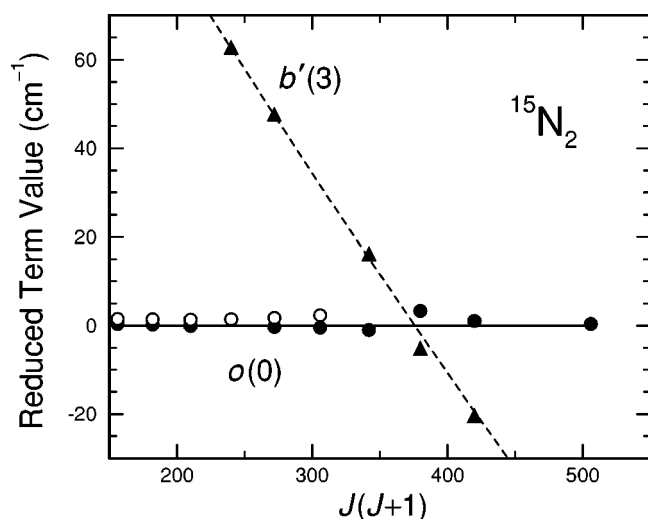


FIG. 8. Reduced term values in the region of the  $o(0)$ - $b'(3)$  crossing [closed circles:  $o(0,e)$ , open circles:  $o(0,f)$ , closed triangles:  $b'(3)$  ( $e$  levels only)], including the results of an effective two-level deperturbation of the  $e$ -level interaction [solid line:  $o(0)$ , dashed line:  $b'(3)$ ]. A quadratic in  $J(J+1)$  has been subtracted from all terms so that the deperturbed  $o(0,e)$  levels lie on the zero line.

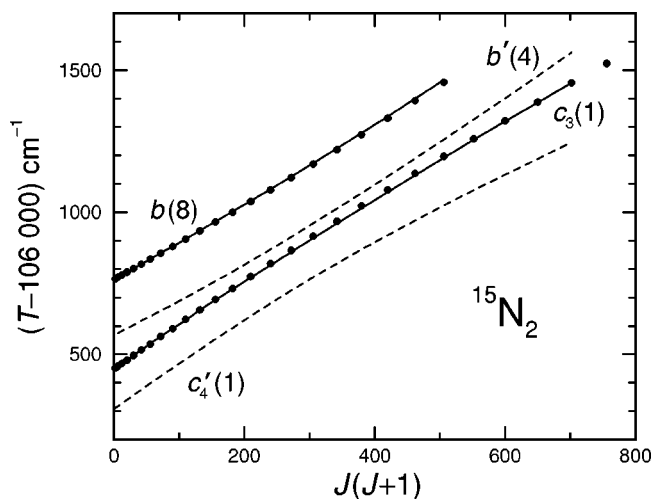


FIG. 9. Experimental rotational term values for the  $c_3(1)$ ,  $b(8)$ ,  $b'(4)$ , and  $c_4'(1)$  states of  $^{15}\text{N}_2$ . Solid curves:  $^1\Pi_u(e)$  levels. Closed circles:  $^1\Pi_u(f)$  levels. Dashed curves:  $^1\Sigma_u^+$  ( $e$  levels only). Strongly-avoided Rydberg-valence crossings occur for each symmetry.

though the experimental data are insufficient to allow one to distinguish between a homogeneous or heterogeneous perturbation, we can safely assume that this  $^1\Sigma_0^-$ - $^1\Pi_1$  interaction is heterogeneous, in which case the deperturbation implies an effective two-level interaction matrix element  $H_{12} = -0.21\sqrt{J(J+1)} \text{ cm}^{-1}$ .

It is well known that it is hazardous to rely on intensities in ionization spectra as indicators of photoabsorption intensities. However, even with this proviso, our spectra indicate an interesting anomaly in the  $R$ -branch intensities associated with the  $o(0)$ - $b'(3)$  crossing region:  $R$ -branch lines in  $b'-X(3,0)$  are excessively weak for excited-state  $J$  values immediately below the crossing region, and are abnormally strong for  $J$  values immediately above the crossing region. It is likely that this is an example of the well-known  $P$ - $R$  intensity anomalies caused by quantum interference between the amplitudes for dipole-allowed transitions into coupled  $^1\Sigma$  and  $^1\Pi$  states, as discussed, e.g., by Lefebvre-Brion and Field.<sup>34</sup> Unfortunately, however, due to limitations in the spectra, we are unable to confirm the opposite intensity behavior expected in the  $b'-X(3,0)$   $P$  branch, and the opposite  $P$ - $R$  behavior expected in the  $o-X(0,0)$  band crossing region.

We note also that we have observed new, weak local perturbations in  $o(0)$ , specifically in the  $J=3e-4e$  region, and also in the  $J=10-14$  region for both the  $e$  and  $f$  levels. These regions were either deperturbed or excluded from the corresponding spectroscopic-parameter fits in Table III. As in the case of  $b(4)$ , we will consider these particular perturbations elsewhere.

### 5. $b(8)$ and $c_3(1)$

Experimental rotational terms for the  $b(8)$ - $c_3(1)$  region are shown in Fig. 9. The  $b(8)$  valence level is perturbed from below by the  $c_3(1)$  Rydberg level, a strongly-avoided crossing between these two levels occurring near  $J=19$  with  $H_{12} = 126 \text{ cm}^{-1}$ . As in the case of the

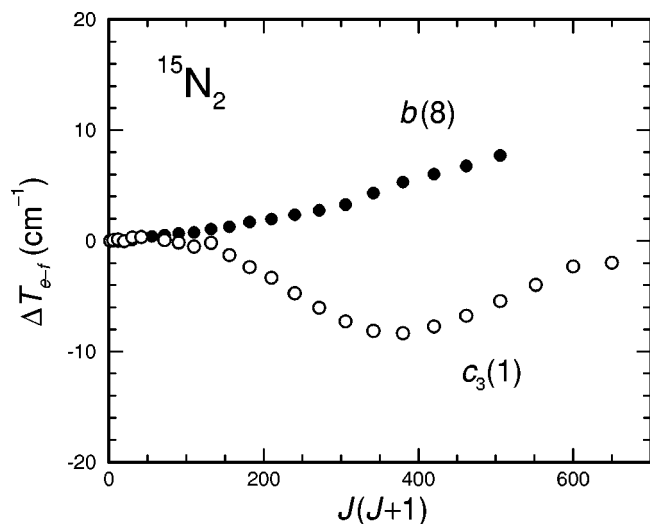


FIG. 10. Observed  $\Lambda$ -doubling in the  $b^1\Pi_u(v=8)$  valence and  $c_3^1\Pi_u(v=1)$  Rydberg states.

$b(5)-c_3(0)$  interaction, significant perturbations occur in the  $B$  values for these levels, the  $D$  value for the lower level  $c_3(1)$  is elevated, the  $D$  value for the upper level  $b(8)$  is large and negative, and additional polynomial terms are required to reproduce the experimental term values. Also shown in Fig. 9 are experimental terms for the  $b'^1\Sigma_u^+(v=4)$  valence level and the  $c_4^1\Sigma_u^+(v=1)$  Rydberg level which play secondary roles in perturbing these  $^1\Pi_u$  states. These  $^1\Sigma_u^+$  levels themselves exhibit a strong mutual homogeneous interaction, resulting in an avoided crossing near  $J=16$  with  $H_{12}=94\text{ cm}^{-1}$ , as is clear from Fig. 9.

In  $^{14}\text{N}_2$ , the  $\Lambda$ -doubling in the  $c_3(1)$  state has been attributed to an interaction with the  $b'(4)$  state.<sup>43</sup> The experimental  $\Lambda$ -doubling in the  $c_3(1)$  and  $b(8)$  states of  $^{15}\text{N}_2$ , shown in Fig. 10, is significant, displaying a degree of complexity well beyond the usual linear dependence on  $J(J+1)$ . In the case of the  $b(8)$  level (closed circles in Fig. 10), the  $\Lambda$ -doubling is primarily caused by heterogeneous interactions with the lower-lying  $c_4'(1)$  and  $b'(4)$  states, the  $b(8,e)$  levels being perturbed upwards with a greater than linear dependence on  $J(J+1)$ . The  $\Lambda$ -doubling in the  $c_3(1)$  level (open circles in Fig. 10) shows clear evidence of being affected by the Rydberg-valence interaction between the  $b'^1\Sigma_u^+(v=4)$  valence and  $c_4^1\Sigma_u^+(v=1)$  Rydberg states which lie above and below  $c_3(1)$ , respectively, post interaction (see Fig. 9), producing perturbations in the  $c_3(1,e)$  levels of opposite signs. For very low  $J$  values, the  $c_3(1,e)$  levels are predominantly perturbed upwards, due to the strong rotational interaction with the  $c_4'(1)$  state which is a member of the same  $p$  complex,<sup>34</sup> despite its lying further away from  $c_3(1)$  than does  $b'(4)$ . On the other hand, for higher  $J$ , as the valence level  $b'(4)$  approaches the Rydberg level  $c_3(1)$  more closely, the predominant effect becomes a downward perturbation of the  $c_3(1,e)$  levels by  $b'(4)$ , this effect maximizing near  $J=19$ , corresponding to the region of closest approach of the  $c_3(1)$  and  $b'(4)$  levels, which do not cross because of the strongly-avoided crossings in both the  $^1\Pi_u$  and  $^1\Sigma_u^+$  levels.

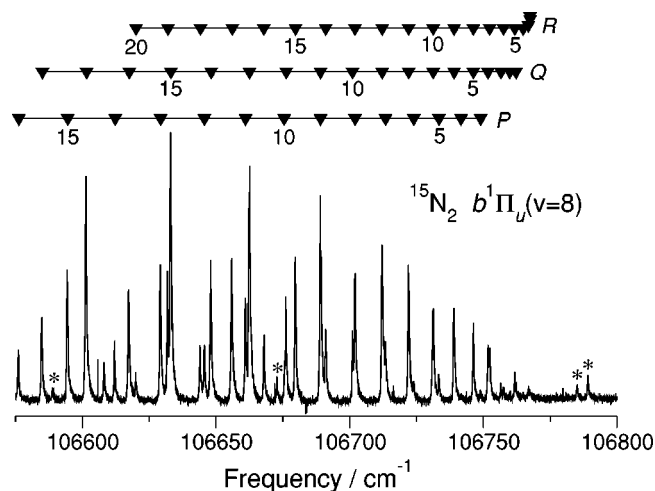


FIG. 11. 1 XUV+1 UV ionization spectrum of the  $^{15}\text{N}_2 b^1\Pi_u-X^1\Sigma_g^+(8,0)$  band, recorded with PDL-based XUV source. Note that the  $R(0)$  and  $P(2)$  lines were not observed. Lines marked with an asterisk are from the  $b'^1\Sigma_u^+-X^1\Sigma_g^+(5,0)$  band:  $P(22)$ ,  $R(25)$ ,  $P(25)$ , and  $P(27)$ , respectively, in order of decreasing energy. Note the ac-Stark-induced asymmetry in the spectral lines.

We note in passing that the slightly scattered points in Fig. 10 at low- $J$  values for the  $c_3(1)$  state result from further weak local perturbations. There appear to be three perturbations in the range  $J < 12$ , in both the  $e$  and  $f$  levels, similar to one of the groups of perturbations observed for  $o(0)$  and mentioned in Sec. VB 4. These perturbations will be analyzed further elsewhere.

There is also a perturbation visible in the intensity distribution of the  $b-X(8,0)$  band, the spectrum of which is shown in Fig. 11. Rotational lines for all branches exciting low- $J$  levels are significantly less intense than rotational lines to higher- $J$  levels, an effect unrelated to laser power levels. This perturbation in intensity occurs due to a destructive quantum-interference effect between the  $^1\Pi_u$  Rydberg and valence transition amplitudes. Vibrational intensity anomalies observed in the  $b-X$  system of  $^{14}\text{N}_2$ ,<sup>44</sup> including an intensity minimum for the  $(8,0)$  band, are known to result from these Rydberg-valence interactions, having been treated successfully semi-empirically by Stahel *et al.*,<sup>10</sup> and by Spelsberg and Meyer using *ab initio* methods.<sup>15</sup> These interference effects have a strong rotational dependence: in the case of  $^{14}\text{N}_2$ , Carroll and Collins<sup>9</sup> note that the intensities of lines in the  $(8,0)$  band with intermediate  $J$  drop markedly before increasing again at higher  $J$ ; in the present case of  $^{15}\text{N}_2$ , evidently the destructive interference effect maximizes at low  $J$ . We have found this observed isotopic and  $J$  dependence to be qualitatively consistent with predictions based on the  $^1\Pi_u$  Rydberg-valence interaction model of Spelsberg and Meyer.<sup>15</sup> The alternative explanation of our observations for  $^{15}\text{N}_2$ , namely that the low- $J$  levels of  $b(8)$  are heavily predissociated due to an accidental perturbation by a short-lived level of another electronic state, is unlikely since no detectable broadening is observed. Furthermore, we know of no such level near the energy of the  $b(8)$  bandhead.

### 6. $b' {}^1\Pi_u(v=9)$ and $o {}^1\Pi_u(v=1)$

In  ${}^{14}\text{N}_2$ , the rotationless  $o(1)$  Rydberg level lies slightly below the  $b(9)$  valence level, the higher Rydberg  $B$  value and homogeneous Rydberg-valence interaction resulting in a weakly-avoided crossing ( $H_{12}=8.1\text{ cm}^{-1}$ ) in the corresponding rotational term series.<sup>20</sup> In  ${}^{15}\text{N}_2$ , the order of these levels is reversed and their energy separation is increased substantially, as illustrated in Fig. 5. As a result, their degree of mutual perturbation decreases significantly and they can, in effect, be regarded as independent levels.

For example, the  $b(9)$  level is very well behaved, with no local perturbations evident in its rotational structure, a  $B$  value appropriate to an unperturbed valence state, a very small  $D$  value, no additional polynomial terms necessary to describe its rotational energies, and negligible  $\Lambda$ -doubling. Similar comments apply to the  $o(1)$  level, where the  $B$  value is typical of an unperturbed Rydberg state, with the exception of a detectable amount of  $\Lambda$ -doubling ( $q < 0$ ), likely caused by heterogeneous interaction with the higher-lying  $b' {}^1\Sigma_u^+(v=6)$  valence level which has a smaller  $B$  value.

### C. The ${}^1\Pi_u$ states of ${}^{14}\text{N}{}^{15}\text{N}$

Practical considerations limit the amount of data obtainable for the mixed isotopomer. For the few  ${}^1\Pi_u$  states of  ${}^{14}\text{N}{}^{15}\text{N}$  studied, the derived spectroscopic parameters in Table IV show the same general behavior as found for  ${}^{14}\text{N}_2$  and  ${}^{15}\text{N}_2$ . For example, the  $b {}^1\Pi_u(v=5)$  and  $c_3 {}^1\Pi_u(v=0)$  states exhibit a strong homogeneous interaction, and a large, negative  $D$  value is found for  $b(5)$ .  $\Lambda$ -doubling is also present in these states, which can be explained in the same way as for  ${}^{14}\text{N}_2$  and  ${}^{15}\text{N}_2$ .

### D. The ${}^1\Sigma_u^+$ states of ${}^{15}\text{N}_2$ and ${}^{14}\text{N}{}^{15}\text{N}$

The  $b' {}^1\Sigma_u^+(v=1)$  states in both  ${}^{15}\text{N}_2$  and  ${}^{14}\text{N}{}^{15}\text{N}$  suffer local perturbation by the  $c_4' {}^1\Sigma_u^+(v=0)$  state. The homogeneous interaction between these two levels has already been examined for  ${}^{14}\text{N}_2$ , in high resolution, by the Amsterdam group<sup>29,37</sup> and by Yoshino *et al.*<sup>22</sup> for the various isotopomers. Narrow spectral lines with the ultrahigh resolution system could only be recorded for the lowest  $J$  values in these two levels, not reaching the avoided-crossing region. Since the lower-resolution data, recorded with the PDL for  $b'(1)$  and higher  $J$  levels of  $c_4'(0)$ , are not more accurate than those of Ref. 22, no attempt was made at an improved analysis of the avoided-crossing region.

Interactions involving several of the higher vibrational levels of the  $b' {}^1\Sigma_u^+$  and  $c_4' {}^1\Sigma_u^+$  states have been discussed in Sec. VB. Overall, the  $B$  values for  $b' {}^1\Sigma_u^+$  increase with  $v$ , contrary to the behavior expected for a normal, unperturbed state. Mixing with the Rydberg state  $c_4' {}^1\Sigma_u^+$  is responsible for this behavior.

## VI. CONCLUSIONS

An XUV-laser-spectroscopic study of the  ${}^1\Pi_u$  and  ${}^1\Sigma_u^+$  states of the isotopomers  ${}^{15}\text{N}_2$  and  ${}^{14}\text{N}{}^{15}\text{N}$  has been performed. New data on 26 absorption bands have been obtained with the highest resolving power and precision

achievable using present-day XUV-laser technology. New molecular spectroscopic parameters and precise isotope shifts have been determined, which will help to inform future models of the molecular structure, interactions, and dynamics of  $\text{N}_2$ .

While the overall pattern of strong Rydberg-valence perturbations in the  ${}^1\Pi_u$  and  ${}^1\Sigma_u^+$  states, together with rotational coupling between the  ${}^1\Pi_u$  and  ${}^1\Sigma_u^+$  manifolds, is found to be similar in  ${}^{15}\text{N}_2$  to that known previously for  ${}^{14}\text{N}_2$ , there are many significantly isotope-dependent aspects. With the aid of a comprehensive perturbation model, which is based on parameters used previously for  ${}^{14}\text{N}_2$  and includes Rydberg-valence interactions and rotational coupling simultaneously, we have found that the present experimental results for  ${}^{15}\text{N}_2$  can be reproduced to a similar level of accuracy as achieved for  ${}^{14}\text{N}_2$ .

In a future publication, experimental studies of the lifetimes of the  ${}^1\Pi_u$  states of the different isotopomers of  $\text{N}_2$  will be presented, providing insight into the isotope dependence of the predissociation behavior for these states. In a further study, the singlet-triplet interactions which are responsible for the several weak local perturbations seen here for the first time in  ${}^{15}\text{N}_2$ , and which have not been reported previously in  ${}^{14}\text{N}_2$ , will be discussed.

## ACKNOWLEDGMENTS

This research has been performed within the Molecular Atmospheric Physics (MAP) program of the Netherlands Foundation for Research of Matter (FOM). The work was supported by the European Community, under the Access to Research Infrastructures initiative of the Improving Human Potential Program, Contract No. HPRI-CT-1999-00064. K.G.H.B. was supported by the Scientific Visits to Europe Program of the Australian Academy of Science.

<sup>1</sup>R. R. Meier, *Space Sci. Rev.* **58**, 1 (1991).

<sup>2</sup>H. Helm, I. Hazell, and N. Bjerre, *Phys. Rev. A* **48**, 2762 (1993).

<sup>3</sup>C. W. Walter, P. C. Cosby, and H. Helm, *J. Chem. Phys.* **99**, 3553 (1993).

<sup>4</sup>H. Lammer, W. Stumptner, G. J. Molina-Cuberos, S. J. Bauer, and T. Owen, *Planet. Space Sci.* **48**, 529 (2000).

<sup>5</sup>M. B. McElroy, Y. L. Yung, and A. O. Nier, *Science* **194**, 70 (1976).

<sup>6</sup>A. O. Nier and M. B. McElroy, *J. Geophys. Res.* **82**, 4341 (1977).

<sup>7</sup>H. Lefebvre-Brion, *Can. J. Phys.* **47**, 541 (1969).

<sup>8</sup>K. Dressler, *Can. J. Phys.* **47**, 547 (1969).

<sup>9</sup>P. K. Carroll and C. P. Collins, *Can. J. Phys.* **47**, 563 (1969).

<sup>10</sup>D. Stahel, M. Leoni, and K. Dressler, *J. Chem. Phys.* **79**, 2541 (1983).

<sup>11</sup>S. A. Edwards, W.-Ü L. Tchang-Brillet, J.-Y. Roncin, F. Launay, and F. Rostas, *Planet. Space Sci.* **43**, 67 (1995).

<sup>12</sup>C. W. Walter, P. C. Cosby, and H. Helm, *J. Chem. Phys.* **112**, 4621 (2000).

<sup>13</sup>W. Ubachs, R. Lang, I. Velchev, W.-Ü L. Tchang-Brillet, A. Johansson, Z. S. Li, V. Likhnygin, and C.-G. Wahlström, *Chem. Phys.* **270**, 215 (2001).

<sup>14</sup>P. K. Carroll and K. Yoshino, *J. Phys. B* **5**, 1614 (1972).

<sup>15</sup>D. Spelsberg and W. Meyer, *J. Chem. Phys.* **115**, 6438 (2001).

<sup>16</sup>M. L. Orlov, J. F. Ogilvie, and J. W. Nibler, *J. Mol. Spectrosc.* **185**, 128 (1997).

<sup>17</sup>J. Bendtsen, *J. Raman Spectrosc.* **32**, 989 (2001).

<sup>18</sup>M. Ogawa, Y. Tanaka, and A. S. Jursa, *Can. J. Phys.* **42**, 1716 (1964).

<sup>19</sup>M. Ogawa, *Can. J. Phys.* **42**, 1087 (1964).

<sup>20</sup>K. Yoshino, Y. Tanaka, P. K. Carroll, and P. Mitchell, *J. Mol. Spectrosc.* **54**, 87 (1975).

<sup>21</sup>D. Mahon-Smith and P. K. Carroll, *J. Chem. Phys.* **41**, 1377 (1964).

<sup>22</sup>K. Yoshino and Y. Tanaka, *J. Mol. Spectrosc.* **66**, 219 (1977).

<sup>23</sup>K. I. Hajim and P. K. Carroll, *J. Phys. B* **20**, 6233 (1987).

<sup>24</sup>P. K. Carroll and K. I. Hajim, *Phys. Scr.* **37**, 682 (1988).

<sup>25</sup>See EPAPS Document No. E-JCPSA6-119-012330 for the rotational line

- assignments and corresponding wave numbers for all bands studied. A direct link to this document may be found in the online article's HTML reference section. The document may also be reached via the EPAPS homepage (<http://www.aip.org/pubservs/epaps.html>) or from <ftp.aip.org> in the directory /epaps/. See the EPAPS homepage for more information.
- <sup>26</sup>W. Ubachs, K. S. E. Eikema, and W. Hogervorst, *Appl. Phys. B: Photophys. Laser Chem.* **57**, 411 (1993).
- <sup>27</sup>W. Ubachs, K. S. E. Eikema, W. Hogervorst, and P. C. Cacciani, *J. Opt. Soc. Am. B* **14**, 2469 (1997).
- <sup>28</sup>K. S. E. Eikema, W. Hogervorst, and W. Ubachs, *Chem. Phys.* **181**, 217 (1994).
- <sup>29</sup>W. Ubachs, *Chem. Phys. Lett.* **268**, 201 (1997).
- <sup>30</sup>S. Gerstenkorn and P. Luc, *Atlas du Spectre d'absorption de la Molécule d'iode 14800–20000 cm<sup>-1</sup>* (CNRS, Paris, 1978).
- <sup>31</sup>I. Velchev, R. van Dierendonck, W. Hogervorst, and W. Ubachs, *J. Mol. Spectrosc.* **187**, 21 (1998).
- <sup>32</sup>S. C. Xu, R. van Dierendonck, W. Hogervorst, and W. Ubachs, *J. Mol. Spectrosc.* **201**, 256 (2000).
- <sup>33</sup>B. Bodermann, H. Knöckel, and E. Tiemann, *Basics and Usage of the Program Iodine Spectrum* (Institut für Quantenoptik Universität Hannover, 1999).
- <sup>34</sup>H. Lefebvre-Brion and R. W. Field, *Perturbations in the Spectra of Diatomic Molecules* (Academic, Orlando, 1986).
- <sup>35</sup>A. Lofthus and P. Krupenie, *J. Phys. Chem. Ref. Data* **6**, 113 (1977).
- <sup>36</sup>C. C. Marston and G. G. Balint-Kurti, *J. Chem. Phys.* **91**, 3571 (1989).
- <sup>37</sup>P. F. Levelt and W. Ubachs, *Chem. Phys.* **163**, 263 (1992).
- <sup>38</sup>P. K. Carroll, C. P. Collins, and K. Yoshino, *J. Phys. B* **3**, L127 (1970).
- <sup>39</sup>W. Ubachs, L. Tashiro, and R. N. Zare, *Chem. Phys.* **130**, 1 (1989).
- <sup>40</sup>W. Ubachs, I. Velchev, and A. de Lange, *J. Chem. Phys.* **112**, 5711 (2000).
- <sup>41</sup>J.-M. Robbe, Ph.D. thesis, Université de Lille, 1978.
- <sup>42</sup>G. Stark (private communication).
- <sup>43</sup>Y. Kawamoto, M. Fujitake, and N. Ohashi, *J. Mol. Spectrosc.* **185**, 330 (1997).
- <sup>44</sup>J. Geiger and B. Schröder, *J. Chem. Phys.* **50**, 7 (1969).